Constant pH Molecular Dynamics Reveals How Proton Release Drives the Conformational Transition of a Transmembrane Efflux Pump

Zhi Yue[†], **Wei Chen**[‡], **Helen I. Zgurskaya**[¶], and **Jana Shen**[†]

[†]Department of Pharmaceutical Sciences, University of Maryland School of Pharmacy, Baltimore, MD 21201

[¶]Department of Chemistry and Biochemistry, University of Oklahoma, Norman, OK, 73019

Abstract

AcrB is the inner-membrane transporter of *E. coli* AcrAB-TolC tripartite efflux complex, which plays a major role in the intrinsic resistance to clinically important antibiotics. AcrB pumps a wide range of toxic substrates by utilizing the proton gradient between periplasm and cytoplasm. Crystal structures of AcrB revealed three distinct conformational states of the transport cycle, substrate access, binding and extrusion, or loose (L), tight (T) and open (O) states. However, the specific residue(s) responsible for proton binding/release and the mechanism of proton-coupled conformational cycling remain controversial. Here we use the newly developed membrane hybridsolvent continuous constant pH molecular dynamics technique to explore the protonation states and conformational dynamics of the transmembrane domain of AcrB. Simulations show that both Asp407 and Asp408 are deprotonated in the L/T states, while only Asp408 is protonated in the O state. Remarkably, release of a proton from Asp408 in the O state results in large conformational changes, such as the lateral and vertical movement of transmembrane helices as well as the salt-bridge formation between Asp408 and Lys940 and other sidechain rearrangements among essential residues. Consistent with the crystallographic differences between the O and L protomers, simulations offer dynamic details of how proton release drives the O-to-L transition in AcrB and address the controversy regarding the proton/drug stoichiometry. This work offers a significant step towards characterizing the complete cycle of proton-coupled drug transport in AcrB and further validates the membrane hybrid-solvent CpHMD technique for studies of proton-coupled transmembrane proteins which are currently poorly understood.
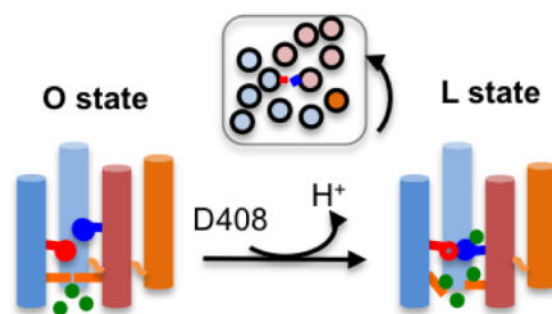
Graphical Abstract

1 Introduction

Multidrug resistance among Gram-negative pathogens is a rising threat to human health. AcrAB-TolC, a tripartite efflux complex from *E. coli*, plays a major role in the intrinsic resistance of Gram-negative bacteria[1,2] by extruding a wide range of toxic substrates and small-molecule compounds from the periplasm or inner membrane to the extracellular space.[3] Within this efflux complex,[4] AcrB is an inner membrane, proton-motive-force dependent pump responsible for substrate binding and initial step in extrusion.[5–8] TolC is an outer membrane channel[9] involved in the final step of substrate extrusion, and AcrA is a periplasmic adaptor protein indispensable for the assembly and function of the complex.[10]

The first high-resolution X-ray crystal structure of AcrB revealed a jellyfish-like homotrimer, comprising TolC-docking (or funnel), porter (or pore) and transmembrane domains.[5] Subsequently, asymmetric crystal structures of AcrB with and without substrates have been solved in the resolution range of 2.5–3.3 Å, revealing protomers in three distinct conformational states of the transport cycle: access, binding and extrusion, according to the state of the substrate-binding pocket.[6–8] These three states are also known as L (loose), T (tight) and O (open) states by drawing analogy to ATP synthase.[11] Consequently, a functional rotation or conformational cycling mechanism was proposed,[6,7] in which substrate recognition and binding occur respectively in the L and T states, followed by a transition to the O state, where substrate extrusion takes place as AcrB cycles back to the L state.[6,7,12] It is believed that the T-to-O transition is energized by proton uptake from periplasm, while the O-to-L transition is triggered by proton release to cytoplasm.[13,14] More recently, X-ray crystallography provided more details of the substrate recognition and binding pathways in the porter domain. Dependent on the molecular mass, drugs can bind first to the access pocket in the L state or directly to the distal pocket in the T state.[15–18]

An important feature of AcrB is the spatial separation between substrate binding and proton translocation – the former takes place in the periplasmic porter domain and the latter in the transmembrane domain.[14,19] The latter contains 12 transmembrane helices (TM), forming two parallel repeats, R1 (TM1, TM3–TM6) and R2 (TM7, TM9–TM12)[19] (Fig. 1a). The flanking helices, TM2 and TM8, connect R1 and R2 to the PN2 and PC2 repeats in the porter domain, respectively,[19] transduce the energy due to proton motive force to the conformational change in the substrate binding pocket. TM4 and TM10 contain Asp407/Asp408 and Lys940, respectively, which form the putative proton binding site,[13,14,20] as they

are the only ionizable residues in the core of the TM domain and their sidechains show significant rearrangements going from the L/T to the O state. In the L and T states, which are similar in the TM domain, both Asp407 and Asp408 form a tight salt bridge with Lys940 (Fig. 1b and Table S4). Asp407 is further stabilized by hydrogen bonding with Thr978 (TM11) and electrostatic interaction with Arg971 (TM11) from a distance of ~7 Å (Fig. 1b and Table S4). By contrast, in the O state, the salt bridge between Asp408 and Lys940 is disrupted (crystallographic distance of ~8.5 Å, see Fig. 1c and Table S4). However, Asp407 maintains a salt bridge with Lys940 (crystallographic distance of ~3.6 Å) but no longer forms a hydrogen bond with Thr978 or interacts with Arg971 (Fig. 1c and Table S4).

Consistent with crystal structure analyses, mutagenesis and functional assay studies suggest that Asp407, Asp408, Lys940 and Arg971 are essential residues for proton transport.[19,21–24] An additional conserved residue Thr978 has also been proposed to play a crucial role.[23,24] Notwithstanding, it remains unclear which specific residue(s) is(are) responsible for proton binding/release. Further, although models have been proposed,[19,25] the detailed mechanism by which proton translocation is coupled to the conformational conversion from T to O and O to L states remains unclear. The objective of this work is to address these two important questions using the state-of-the-art continuous constant pH molecular dynamics (CpHMD) simulations.

Recently, Poisson-Boltzmann (PB) and free energy based methods were used in combination with conventional MD to determine the protonation states of essential residues.[19] This study ruled out the possibility of deprotonation of Lys940 and Arg971, and suggested a two proton model, in which Asp407 and Asp408 are deprotonated in the L/T states and protonated in the O state.[19] Deprotonation of Asp407/Asp408 in the L/T states is congruent with the salt bridges with Lys940 present in the crystal structures (Fig. 1a and Table S4), and protonation of Asp407 in the O state is supported by a hydrogen bond between the carboxyl oxygen and the backbone carbonyl oxygen of Gly403 in the highest resolution crystal structures (Table S5), although Asp407 is also within a salt-bridge distance from Lys940 (Table S4). The two proton model however contradicts another recent MD study which showed that protonation of both Asp407 and Asp408 destabilizes the O state.[25] By testing a combination of protonation states of Asp407/Asp408 for the O protomer, the latter study supported a one proton model, in which protonation and deprotonation of Asp408 alone drives the conformational cycling of AcrB.[25]

Intrigued by the above controversy and the outstanding question regarding the mechanism of conformational cycling, we set out to investigate the proton-coupled conformational dynamics of the TM domain of AcrB using the continous constant pH MD (CpHMD).[26,27] Conventional MD, which has been used in all previous MD studies of AcrB,[18,19,25,28] assumes fixed protonation states. By contrast, CpHMD allows ionizable residues to titrate during dynamics in response to changes in the conformational environment and solution pH. Thus, CpHMD affords a more realistic description of pH-dependent dynamics and more accurate pK_a calculations.[29] The calculated macroscopic pK_a's naturally incorporate the effect of dielectric relaxation without the need for an effective dielectric constant as in traditional PB electrostatic calculations.[30–32] For pK_a calculations, CpHMD also holds advantage over the traditional free energy methods such as free energy perturbation and

thermodynamic integration, as CpHMD gives all pK_a's in one simulation while the latter can give only one pK_a, while fixing the protonation states of all other titratable sites.

Due to the direct coupling between protonation-state changes and conformational dynamics in CpHMD, an enhanced sampling method, such as the temperature[33] or pH replica-exchange (REX) protocol[27] needs to be employed to ensure pK_a convergence on a nanosecond time scale.[27] As other Hamiltonian replica-exchange methods, the pH-REX protocol uses random walks on different potential energy surfaces to accelerate crossing of local energy barriers.[27] Previous work by us[27] and others[34,35] demonstrated a significant reduction in random errors and rapid pK_a convergence, which would not be possible with independent trajectories at single pH conditions.

The present work employs the most recently developed membrane-enabled hybridsolvent CpHMD method with pH-REX,[27,36] which propagates the conformational dynamics of the transmembrane protein in explicitly solvated lipid bilayer and titration dynamics using a membrane generalized Born implicit-solvent model.[37] This technique opened a door to new mechanistic insights for transmembrane channels[38] and transporters.[36] Here, CpHMD simulations of the O protomer reveal pH-dependent conformational changes towards the L state, which can be attributed to the deprotonation of Asp408. Thus, our work lends support to the one-proton model and offers an intimate view of how proton release induces the conformational cycling event of AcrB.

2 Results and Discussion

CpHMD simulations were performed on the TM domains (where proton translocation takes place) of the separate L, T and O protomers in AcrB, with initial coordinates taken from the 1.9-Å-resolution crystal structure (pdb id: 4DX5[16]). Truncation of the system ensures adequate sampling of the region of interest such that large conformational dynamics can be observed. The trimer interface in the transmembrane region is minimal[5] and currently no evidence suggests it affects proton binding/release. The porter domain was removed, as drug transport is spatially separated from proton translocation. We note that the system truncation will not affect the pK_a's discussed. The caveats of the system size reduction will be discussed in Concluding Discussion.

Simulations made use of the pH-REX protocol,[27] which contained 24 pH replicas in the pH range between 1 and 8.5. A pH swap was attempted every 500 MD steps. Each replica was subject to constant NPT molecular dynamics for 35–40 ns, resulting in the aggregate sampling time of 840–960 ns. Based on convergence analysis, data from the first 20 ns of each replica were discarded. Owing to the coupling of titration and conformational dynamics in CpHMD, the pH-REX protocol accelerates the sampling of not only protonation but also conformational states.[27] Our recent pH-REX simulations of a transmembrane protein showed that the conformational changes produced by 20 ns per replica sampling (400 ns aggregate time) are similar to those from the conventional fixed-protonation-state trajectories of 1 μs.[36] This is however not surprising, given that temperature REX simulations have been demonstrated to offer a ten-fold acceleration in protein folding simulations.[39] Thus, we expect the current simulations to produce conformational changes

comparable to single pH (or fixed-protonation-state) trajectories with at least a ten-fold increase in length, i.e., 350–450 ns.

O protomer undergoes a pH-dependent backbone conformational change

A backbone conformational change involving a relative motion between R1 and R2 repeats was evident at high pH conditions in the O protomer simulations (Fig. S1). To examine the pH dependence, we aligned R1 and calculated the probability distribution (histogram) of the R2 backbone root-mean-square deviation (rmsd) from the starting structure for different pH conditions. The distribution is centered around 2.2 Å at and below pH 4, while a second peak appears round 3.8 Å at pH 4.5 and 5. At and above pH 6, the first peak disappears, while the second peak remains in the same location (Fig. 2a). This plot indicates that the O protomer maintains the native conformation at low pH but samples a new state (denoted O^*) at increased pH. We calculated the occupancy of O^* state as a function of pH using an rmsd cutoff of 4 Å (the upper boundary of the O-state distribution). Interestingly, a sigmoidal curve with a transition midpoint around pH 4.5 was revealed (Fig. 2b). The occupancy is low, as the system requires much longer time (compared to the simulation length) to complete the conformational change. In contrast to the O protomer, no significant backbone conformational change was observed in the simulations of the L and T protomers (see Concluding Remarks). Thus, in the remainder of the work, we will focus the discussion on the O-protomer simulations.

Lateral R2/R1 rotation at high pH resembles the O-to-L transition

To visualize the conformational change, we overlaid the trajectory snapshots with the lowest and highest rmsd. With R1 aligned to the starting structure, we noticed an anti-clockwise lateral rotation of R2 (Fig. 2c), similar to the shear motion of R2/R1 in the O-to-L transition described by Eicher *et al.* based on the crystal structures.[19] The resemblance is supported by a principal component analysis, in which the trajectories at different pH were projected onto the first principal component of the O-to-L transition based on 16 crystal structures (Fig. S2). To further examine the collective movement of R2, we projected the centers of mass of TM helices onto the membrane plane following the alignment of R1. Consistent with the visual evidence (Fig. 2c), anti-clockwise lateral displacements are apparent for all R2 helices (Fig. 2d).

TM4, TM5, TM8 and TM10 show significant pH-dependent backbone conformational change

To examine the backbone conformational change of individual TM helices, we calculated their rmsd distributions from the starting structure while aligning all TM helices to the starting structure. For comparison, rmsd between the L and O protomers in the crystal structures were obtained using the same protocol. Interestingly, the distributions revealed significant pH-dependent rmsd increase for TM5, TM10, TM4 and TM8 (in the descending order, see Fig. 3a–d and Fig. S3). TM4 and TM10 are two helices that carry the essential residues Asp407/Asp408 and Lys940, while TM5 and TM8 are two helices that form extensive hydrophobic contacts with TM10 (Fig. 2c). Remarkably, these helices, in particular TM5 and TM8, also show significant rmsd between the O and L protomers in the crystal structures (Fig. 3e and Table S3). Thus, at the individual helix level, the pH-induced

backbone conformational changes in the O protomer are largely in agreement with the O-to-L transition based on the crystallographic data.

Essential-residue interactions at high pH resembles the L state

To further test if the pH-induced conformational changes in O protomer represent the transition to L state, we examined the characteristic sidechain-to-sidechain distances involving essential residues Asp407, Asp408, Lys940, Thr978 and Arg971. Distribution of the Asp408–Lys940 distance shows a peak at ~9 Å at low pH (Fig. 4a), consistent with the crystal structures of the O protomer (Table S4). Above pH 4, the major peak is centered at 3 Å, indicating the formation of a salt bridge (Fig. 4a), which agrees with the crystal structures of L protomer (Table S4).

High pH also strengthens the salt-bridge interaction between Asp407 and Lys940, as evident from the increased intensity of the peak i.e., more frequent sampling (Fig. 4b), consistent with a 0.5-Å decrease comparing the average crystallographic distances in the O and L protomers (Table S4). It is worth commenting on the salt bridge between Asp407 and Lys940 in the O state, as in some crystal structures, e.g., pdb id 4DX5, Asp407 forms a hydrogen bond with Gly403 (absent in other crystal structures, Table S5), while its distance to Lys940 is slightly larger (4.1 *vs.* an average of 3.6 Å for all crystal structures, Table S4). In our simulations, the Asp407–Gly403 hydrogen bond was unstable and a closer average distance was sampled between Asp407 and Lys940 (Fig. 4b). These differences can be readily understood, as a crystal structure represents a local energy minimum under a certain crystalline environment, while MD samples an ensemble of configurations. Next we examined the distance between Asp407 and Asp408. As pH increases, the peak is moved from 6.5 to 4.5 Å (Fig. 4c), in accord with the difference between the O and L protomers in the crystal structures (Table S4).

Another characteristic of the O-to-L transition is the breakage of the hydrogen bond between Lys940 and Thr978, which is often present in the crystal structures of O protomer (Table S4). Our simulations showed frequent sampling of the hydrogen bond at low pH, while as pH increases above pH 4, the Lys940–Thr978 distance increases beyond 6 Å, consistent with the changes in the crystal structures (Table S4) as well as the simulations by Yamane *et al.* using deprotonated Asp407 and Asp408.[25]

Additionally, we examined how high pH induces an attraction between Asp407 and Arg971 (Fig. S4). As pH is increased from 3 to 6, the peak moves from ~12.5 Å to 6–9 Å, consistent with the changes in the crystal structure distances Table S4). Taken together, the data show that the sidechain interactions among essential residues at pH above 4 where O* state is favored (Fig. 4e) are very similar to those in the crystal structure of L protomer (Fig. 1b).

Since Asp408 deprotonates in the O-to-L transition (see later discussion), we hypothesized that its attraction to Lys940 drives the aforementioned sidechain rearrangements. To test it, the instantaneous distance between Asp408 and Lys940 is plotted against the distance between Asp407 and Asp408 and between Lys940 and Thr978. As Asp408 and Lys940 move closer, the Asp407–Asp408 distance decreases, while the Lys940– Thr978 distance increases (Fig. 4f). The apparent correlation and anti-correlation seen here are consistent

with the salt-bridge formation being a driving force for the changes in the essential-residue interactions.

Asp407 and Asp408 are deprotonated in the L and T states

The calculated microscopic pK_a's of Asp407/Asp408 are similarly depressed, 2.2/3.0 in the L and 2.6/2.8 in the T state (Table 1), consistent with the presence of salt bridges between Lys940 and Asp407/Asp408 in the crystal structures (Table S4). Note, Lys940 was charged in the entire simulation pH range (1–8.5), consistent with the previous PB calculation.[19] Thus, our simulations confirm the crystal-structure-based consensus that Asp407/Asp408 are deprotonated in L and T states,[13,14,20] in agreement with the previous computational studies. [18,19]

Due to the similar pK_a's and close proximity (< 5 Å, Fig. 4c), protonation/deprotonation of Asp407 and Asp408 in the L and T states is strongly coupled. As such Asp407/Asp408 should be considered together as a dyad and its titration can be described by a stepwise model which yields two macroscopic pK_a's. Accordingly, starting from the doubly deprotonated state, the first/second protonation events have the pK_a's of 3.4/1.9 for the L state, and 3.4/1.8 for the T state (Table 1 and Fig. 5a). Notice that the two protonation steps are separated by more than 1.5 pH units, which indicates that in the transition from T to O state binding of one proton is much more likely than the binding of two protons.

Asp408 takes up a proton in the T-to-O transition

Upon transition from the T to the O state, the pK_a of Asp408 increases by 2.2 units to 5, while the pK_a of Asp407 increases by 0.8 units to 3.4 (Table 1). Thus, having a large pK_a shift and a higher pK_a value in the O state, Asp408 is more likely to become protonated at periplasmic pH ~6[40] compared to Asp407. This also means that Asp408 is the only proton donor in the O state, consistent with the drastically different crystallographic distances in the O protomer, e.g., 3.6±0.6 Å for Asp407–Lys940 and 8.5±0.5 Å for Asp408–Lys940 (Table S4). We note that the pK_a of Asp408 is 0.4 and 0.2 units higher than Asp407 in the L and T states, respectively. Although these differences are small (block standard error of 0.1 units, see Table 1), they are in agreement with Asp408 having a high affinity for protons.

We note that our calculated pK_a's are systematically underestimated by perhaps two units due to the use of the generalized Born (GB) implicit-solvent model for driving the protonation dynamics.[27,36,41] However, this limitation does not impact the pK_a differences between the two residues and the pK_a changes between the different states.[36,41]

Proton release from Asp408 drives the O-to-L transition

If Asp408 was indeed the proton binding residue, its deprotonation would induce the O-to-L transition and its pK_a would drop to the L-state value after the transition. To test this, we compared the pH profiles of Asp408 titration and the O^*-state occupancy. The deprotonation of Asp408 occurs in the same pH range (3 to 6) as the increase of the O^*-state occupancy (Fig. 5c and Fig. 5d, brown). Importantly, Asp407 remains largely deprotonated above pH 3. The pH profile of Asp408 deprotonation also matches that of the salt-bridge formation

between Asp408 and Lys940 (Fig. 5d, black), which correlates with other sidechain movements towards the L configuration (Fig. 4f).

Now we examine the pK_a change accompanying the conformational change from O to O* state. The microscopic pK_a of Asp408 decreases from 5.0 to 3.1. The latter is similar to the pK_a of 2.8 in the L state (Table 1). We note, the remaining difference of 0.3 units is likely the result of incomplete conformational conversion due to the significantly short simulation time. Thus, both conformational and pK_a data suggest that deprotonation of Asp408 induces the O-to-L transition.

Disruption of hydrophobic contacts facilitates water access to the core

Considering deprotonation of Asp408 requires water entrance from the cytoplasm, we examined water dynamics in the simulation. Consistent with the finding by Eicher et al.,[19] the periplasmic side of the TM domain of O protomer is completely sealed, while water can access from the cytoplasmic side (Fig. 6a). We calculated the number of water along the membrane normal as a function of pH. At low pH, there is at most one water near Asp407/Asp408/Lys940, while above pH 4, additional water molecules are found (Fig. 6a). Thus, high pH induces hydration of the proton binding site.

Three and four amino acids below Asp408 and Lys940 on TM4 and TM10, respectively, are two hydrophobic residues Val411 and Leu944 that make contact in the crystal structure, blocking water entrance from cytoplasm. Since the region around this hydrophobic constriction becomes hydrated above pH 4 (Fig. 6a), we speculated that the Val411–Leu944 contact breaks at high pH. To test this, the distribution of the Val411– Leu944 minimum sidechain distance was plotted as a function of pH. Below pH 4, the distribution is broad with the maximum spanning 4.5–7 Å (Fig. 6b), indicating that the hydrophobic contact opens from time to time, which explains the presence of a single water in the core at low pH. However, above pH 4, the distribution exhibits two peaks, a minor one at 4 Å and a major one at 7 Å (Fig. 6b). This indicates that most of the time the hydrophobic contact is broken, which explains the increased core hydration at high pH.

In addition to the interaction with Val411, Leu944 on TM10 is also engaged in a strong hydrophobic contact with Ile445 on TM5, which becomes disrupted from time to time as pH is raised above 4 (Fig. 6c). Furthermore, the hydrophobic interaction between Val448 on TM5 and Ile943 on TM10 is also weakened at high pH (Fig. S5). The weakened hydrophobic association between TM5 and TM10 leads to a significantly increased number of water near Ile445 and Leu944 (Fig. S6), and is another facilitator for the increased core hydration at high pH. We suggest the above pH-dependent dynamical behavior may also contribute to the unexpectedly high rmsd of TM5, as observed in our simulations and crystal structures (Fig. 3b and e).

Since the disruption of the hydrophobic contacts occurs in the same pH-dependent manner as the formation of the Asp408–Lys940 salt bridge, we asked whether the two events occur concomitantly. Plotting the instantaneous distance of Asp408 to Lys940 *vs.* that of Val411 to Leu944 confirms the correlation, e.g., when a tight salt bridge is formed between Asp408 and Lys940, the hydrophobic contact between Val411 and Leu944 is broken (Fig. S7). The

correlation is also evident from the simulation snapshots. At pH 4, protonated Asp408 and Lys940 point away from each other, while Val411 and Leu944 form a hydrophobic constriction and few water molecules are seen (Fig. 6d). At pH 6, deprotonated Asp408 forms a salt bridge with Lys940, while the hydrophobic contacts are broken and many water molecules enter the site (Fig. 6e).

TM8 may transmit the pH-induced conformational changes to the porter domain

One important question concerns how the proton-motive force driven conformational changes in the TM domain is propagated to the periplasmic porter domain to enable substrate extrusion. In the absence of the porter domain, we explored the question by examining the center-of-mass (COM) movement of TM2 and TM8 which connect the two domains. TM8, which shows a more significant pH-induced backbone conformational change than TM2 (Fig. 3c), moves towards cytoplasm by nearly 1 Å as pH is increased from 3 to 6 (Fig. 7a), consistent with the difference between the O and L protomers in the crystal structures (Table S6). By contrast, the vertical movement of TM2 is negligible in the simulation, although it is equally noticeable in the crystal structures (Table S6).

We suspected that the vertical movement of TM8 is related to that of TM10, as the two helices are associated via several strong hydrophobic contacts (e.g., Tyr877–Leu931, Leu881–Ile935 and Leu888–Ile943), and TM10 also moves down with increasing pH (by about 0.5 Å at pH 6, see Fig. 7a). Indeed, plotting the z positions of TM8 and TM10 reveals a strong correlation (Fig. 7b). We further examined the movement of TM8 in the membrane plane. In contrast to TM10, which does not display a significant pH-dependent change, TM8 moves by about 0.6 and 0.3 Å in the x and y directions, respectively. The x-direction movement agrees with the O-to-L transition in the crystal structures; however, the y-direction is much smaller in magnitude and has an opposite sign (Table S6). Nonetheless, from the periplasmic view, TM8 appears to move away from the R1–R2 interface at increasing pH (Fig. 2d), which agrees with the description by Eicher *et al.*[19] We note that although the above data are interesting, they should be taken with a grain of salt due to the lack of porter domain, which may affect the TM motion, and the pronounced fluctuation of the TM positions (about 1 Å, see Fig. S15).

Concluding Discussion

CpHMD simulations initiated from the O crystal structure of AcrB revealed large backbone and sidechain conformational changes due to the deprotonation of Asp408 while Asp407 remains in the charged state. R2 helices collectively rotate about R1 in the anti-clockwise direction on the membrane plane (Fig. 8a), resembling the O-to-L transition revealed by the crystal structures and discussed by Eicher *et al.*[19] Such backbone movements were not reported by the previous all-atom simulations;[19,25] however, similar motion has been observed in the most recent hybrid coarse-grained simulations.[42] Along with the backbone changes, the sidechains of essential residues, Asp407, Asp408, Lys940, Thr978 and Arg941 rearrange, which leads to, among others, the movement of Lys940 from Thr978 to Asp408. The latter in agreement with the simulation by Yamane *et al.* using deprotonated Asp407/Asp408 for the O protomer.[25] Concomitant with these pH-induced conformational changes,

hydrophobic interactions between the R1 and R2 helices are disrupted or weakened, allowing cytoplasmic water to access the core, facilitating proton release (Fig. 8b). Further, our simulations showed that TM8 moves vertically towards cytoplasm and laterally away from the R1–R2 interface at increasing pH, largely consistent with the crystal structures (Fig. 7). Since TM8 is connected to the more rigid PC2/PN1 repeat in the porter domain,[19] these movements may be a major contributor to the large conformational changes which ultimately leads to substrate extrusion.[14]

The resemblance between the aforementioned pH-induced conformational changes and the O-to-L transition from the crystal structure data lends support to the one proton model emerged from our simulation, i.e., in the O state Asp407 is deprotonated and proton release from Asp408 at cytoplasmic pH drives the transition to the L state. Further, our data ruled out the two proton model, as the 1.5-unit splitting in the stepwise pK_a's of the T state suggests that only one proton is taken up in the T-to-O transition. Additionally, the pK_a of Asp408 increases by two units going from T to O state suggests Asp408 is the residue that takes up the proton. The pK_a decrease of two units in the O-to-O* transition suggests Asp408 is the residue that releases the proton. Our data is also consistent with the MD study by Yamane *et al.*, which demonstrated that the O state becomes unstable when both Asp407 and Asp408 are protonated.[25]

Based on the PB and free energy calculations using static structures, Eicher *et al.* obtained pK_a's of ~8.2/10.8 for Asp407/Asp408, supporting a two-proton model, i.e., both 20 Asp407 and Asp408 are protonated in the O state and their deprotonation leads to the transition to the L state.[19] Note, the order of pK_a's indicates that Asp408 has a higher proton affinity, in agreement with the present work; however, the pK_a's are signficantly upshifted. We suggest that the PB-derived pK_a's are overestimated, similarly as other PB calculations for deeply buried residues due to the neglect of ionization-induced conformational relaxation.[31,36] Had this overestimation been accounted for, the two computational studies would have suggested the same proton model. We note, since both studies used charged Asp407 and Asp408 for the L state, the hydration pathways are in general agreement.

Turning to the hybrid-solvent CpHMD employed in the present study, we note that it systematically underestimates the pK_a shifts of buried residues, such as Asp407 and Asp408, although we believe the relative order of pK_a's is robust based on the previous validation studies.[27,36,41] Another limitation of CpHMD is the neglect of quantum effects, which can be significant for highly coupled residues in close proximity such as Asp407 and Asp408 in the L/T state. Quantum effects may be required to capture the fine difference between Asp407 and Asp408 in the T state such that Asp408 captures the first proton thereby inducing the T-to-O transition, which was not observed in the current study (more see below).

In addition to the aforementioned methodological limitations, a major caveat of the present study is the time scale of the CpHMD simulations (close to 1 μs aggregate time), which is several orders of magnitude below that of the real biological events. This may be a major contributor to the discrepancy between the O* state and the L state in the crystal structures. Other caveats are related to the truncation of the porter domain and separation of the trimer

to three protomers, which ensures adequate sampling of the region of interest such that large conformational changes can be observed within the limited simulation time. Although truncation of the porter domain is justified by the spatial separation between drug binding and proton translocation, the lack of porter domain may affect the dynamics of TM2 and TM8 and contribute to the deviation between the O^* state and the L state in the crystal structures. It may also be another factor for the absence of conversion from T to O state in our current simulations, since substrate binding may be required for the conformational change.[14] Without the porter domain, separation of the trimer into single monomers is a reasonable approximation, as the trimer interface in the membrane is minimum.[5] Note, however, the interface between the porter domain monomers is extensive and cysteine linking experiments showed concerted dynamics.[43]

AcrB is a prototype for RND superfamily of multidrug transporters. Exploiting recent crystal structures of AcrB, the present study offered a novel, dynamic view of how proton release drives the O-to-L conformational transition, and addressed the controversy regarding stoichiometry. While further validation by computational studies and experiments are needed, the new insights will facilitate the understanding of other RND transporters, such as MexB, MtrD, CusA and ZneA, which share high structural similarity with AcrB.[44] Future work will include the implementation of GPU-accelerated CpHMD simulations to significantly extend the trajectory length and system size. The speed up would also allow the application of all-atom CpHMD with particle mesh Ewald electrostatics, which is more accurate but requires ten times longer simulation to reach protonation-state convergence. [45] Thus, the present work paves the way for exciting future studies aimed at detailed elucidation of the drug-proton antiport in the complete conformational cycle of AcrB.

Materials and Methods

Three simulation systems were prepared, corresponding to the transmembrane domains (residues 1–29, 334–558, 873–1033) of the L, T and O protomers in the asymmetric crystal structure of AcrB (pdb id: 4DX5, resolution 1.6 Å).[16] The TM domains of L, T and O protomers were inserted in an explicit bilayer of POPE (1-palmitoyl-2-oleoyl-*sn*-glycero-3-phosphoethanolamine) lipids. A 15-Å water layer was added to the top and bottom of the bilayer. Na^+ and Cl^- ions were added to the bulk water to achieve a charge neutral condition in the restrained equilibration. More ions were added to arrive at an ion concentration of 150 mM.

Unless otherwise stated, simulations employed the CHARMM package (version c37a2).[46] The protein, lipids and water were represented by CHARMM22/CMAP,[47,48] CHARMM36[49] and CHARMM modified TIP3P model,[46] respectively. Simulations were conducted in four stages. In the first stage, an initial 500-ps restrained equilibration with fixed protonation states was carried out to relax the system following the CHARMM-GUI protocol.[50,51] In the second stage, the lipid bilayer was equilibrated for about 100 ns with fixed protonation states using the GROMACS MD package (version 5.0).[52] In the third stage, the entire system was equilibrated at a single pH (crystallization pH 6.5) using the membraneenabled[36] hybrid-solvent[27] CpHMD method[26,33] (PHMD module in CHARMM).

In the final stage, production simulations were performed using the above CpHMD method with the pH replica exchange (pH-REX) protocol[27] (module REPDSTR).

Based on the idea of λ dynamics,[53] CpHMD makes use of a set of continuous titration coordinates to enable protonation/deprotonation of an arbitrary number of ionizable sites at a specified solution pH in the course of molecular dynamics simulation.[26,54] In the membrane-enabled hybrid-solvent scheme,[27,36] conformational dynamics of the protein is calculated using an explicit bilayer, while the titration coordinates are updated using the GBSW implicit-solvent model[55] with an implicit membrane.[37] The implicit membrane was excluded from the λ dynamics calculation for the protein interior residues by placing a cylinder with a radius of 25 Å centered in the protein, following our previous work.[36]

In the CpHMD simulations, all Asp, Glu, His and Lys sidechains were allowed to titrate. The pH REX protocol employed 24 replicas assigned with starting pH conditions of pH 1 to 5 with a spacing of 0.25 unit and pH 5 to 8.5 with a spacing of 0.5 unit. The pH range 1– 8.5 covers the peri- and cytoplasmic pH and allows complete protonation/deprotonation of Asp407 and Asp408 which is the key interest of the study. The low and high pH condition were included to facilitate barrier crossing. A smaller pH interval (i.e. more pH replicas) was used for pH 1–5 in order to increase the exchange acceptance ratio, which would be otherwise low due to the titration of a large number of acidic residues.[56] This is similar to temperature REX simulations, where the number of replicas in a given temperature range increases with the square root of the degrees of freedom.[57,58] Each replica underwent constant NPT MD at 310 K and 1 atm pressure for 35 and 40 ns for L/T and O protomers, respectively, resulting in the aggregate sampling time of 840 ns and 960 ns, respectively. A pH exchange was attempted every 500 MD steps (1 ps), with an acceptance rate of at least 40%. More detailed simulation protocols and additional analyses are given in Supplementary Information.

Supplementary Material

Refer to Web version on PubMed Central for supplementary material.

Acknowledgments

References

1. Nikaido H. Multidrug Resistance in Bacteria. Annu Rev Biochem. 2009; 78:119–146. [PubMed: 19231985]

2. Li XZ, Plésiat P, Nikaido H. The Challenge of Efflux-Mediated Antibiotic Resistance in Gram-Negative Bacteria. Clin Microbiol Rev. 2015; 28:337–418. [PubMed: 25788514]

3. Okusu H, Ma D, Nikaido H. AcrAB efflux pump plays a major role in the antibiotic resistance phenotype of Escherichia coli multiple-antibiotic-resistance (Mar) mutants. J Bacteriol. 1996; 178:306–308. [PubMed: 8550435]

4. Du D, Wang Z, James NR, Voss JE, Klimont E, Ohene-Agyei T, Venter H, Chiu W, Luisi BF. Structure of the AcrAB-TolC multidrug efflux pump. Nature. 2014; 509:512–515. [PubMed: 24747401]

5. Murakami S, Nakashima R, Yamashita E, Yamaguchi A. Crystal structure of bacterial multidrug efflux transporter AcrB. Nature. 2002; 419:587–593. [PubMed: 12374972]

6. Murakami S, Nakashima R, Yamashita E, Matsumoto T, Yamaguchi A. Crystal structures of a multidrug transporter reveal a functionally rotating mechanism. Nature. 2006; 443:173–179. [PubMed: 16915237]

7. Seeger MA, Schiefner A, Eicher T, Verrey F. Structural asymmetry of AcrB trimer suggests a peristaltic pump mechanism. Science. 2006; 313:1295–1298. [PubMed: 16946072]

8. Sennhauser G, Amstutz P, Briand C, Storchenegger O, Grütter MG. Drug export pathway of multidrug exporter AcrB revealed by DARPin inhibitors. PLoS Biol. 2007; 5:e7. [PubMed: 17194213]

9. Koronakis V, Sharff A, Koronakis E, Luisi B, Hughes C. Crystal structure of the bacterial membrane protein TolC central to multidrug efflux and protein export. Nature. 2000; 405:914–919. [PubMed: 10879525]

10. Mikolosko J, Bobyk K, Zgurskaya HI, Ghosh P. Conformational flexibility in the multidrug efflux system protein AcrA. Structure. 2006; 14:577–587. [PubMed: 16531241]

11. Yoshida M, Muneyuki E, Hisabori T. ATP synthase – a marvellous rotary engine of the cell. Nat Rev Mol Cell Biol. 2001; 2:669–677. [PubMed: 11533724]

12. Seeger MA, von Ballmoos C, Eicher T, Brandstatter L, Verrey F, Diederichs K, Pos KM. Engineered disulfide bonds support the functional rotation mechanism of multidrug efflux pump AcrB. Nat Struct Mol Biol. 2008; 15:199–205. [PubMed: 18223659]

13. Murakami S. Multidrug efflux transporter, AcrB - the pumping mechanism. Curr Opin Struct Biol. 2008; 18:459–465. [PubMed: 18644451]

14. Pos KM. Drug transport mechanism of the AcrB efflux pump. Biochim Biophys Acta. 2009; 1794:782–793. [PubMed: 19166984]

15. Nakashima R, Sakurai K, Yamasaki S, Nishino K, Yamaguchi A. Structures of the multidrug exporter AcrB reveal a proximal multisite drug-binding pocket. Nature. 2011; 480:565–569. [PubMed: 22121023]

16. Eicher T, jea Cha H, Seeger MA, Brandstätter L, El-Delik J, Bohnert JA, Kern WV, Verrey F, Grütter MG, Diederichs K, Pos KM. Transport of drugs by the multidrug transporter AcrB involves an access and a deep binding pocket that are separated by a switch-loop. Proc Natl Acad Sci USA. 2012; 109:5687–5692. [PubMed: 22451937]

17. Nakashima R, Sakurai K, Yamasaki S, Hayashi K, Nagata C, Hoshino K, Onodera Y, Nishino K, Yamaguchi A. Structural basis for the inhibition of bacterial multidrug exporters. Nature. 2013; 500:102–106. [PubMed: 23812586]

18. Yao XQ, Kimura N, Murakami S, Takada S. Drug Uptake Pathways of Multidrug Transporter AcrB Studied by Molecular Simulations and Site-Directed Mutagenesis Experiments. J Am Chem Soc. 2013; 135:7474–7485. [PubMed: 23627437]

19. Eicher T, Seeger MA, Anselmi C, Zhou W, Brandstätter L, Verrey F, Diederichs K, Faraldo-Gómez JD, Pos KM. Coupling of remote alternatingaccess transport mechanisms for protons and substrates in the multidrug efflux pump AcrB. eLife. 2014; 3:e03145.

20. Du D, van Veen HW, Murakami S, Pos KM, Luisi BF. Structure, mechanism and cooperation of bacterial multidrug transporters. Curr Opin Struct Biol. 2015; 33:76–91. [PubMed: 26282926]

21. Guan L, Nakae T. Identification of Essential Charged Residues in Transmembrane Segments of the Multidrug Transporter MexB of *Pseudomonas aeruginosa*. J Bacteriol. 2001; 183:1734–1739. [PubMed: 11160105]

22. Su CC, Li M, Gu R, Takatsuka Y, McDermott G, Nikaido H, Yu EW. Conformation of the AcrB multidrug efflux pump in mutants of the putative proton relay pathway. J Bacteriol. 2006; 188:7290–7296. [PubMed: 17015668]

23. Takatsuka Y, Nikaido H. Threonine-978 in the Transmembrane Segment of the Multidrug Efflux Pump AcrB of *Escherichia coli* Is Crucial for Drug Transport as a Probable Component of the Proton Relay Network. J Bacteriol. 2006; 188:7284–7289. [PubMed: 17015667]

24. Seeger MA, von Ballmoos C, Verrey F, Pos KM. Crucial role of Asp408 in the proton translocation pathway of multidrug transporter AcrB: Evidence from sitedirected mutagenesis. Biochemistry. 2009; 48:5801–5812. [PubMed: 19425588]

25. Yamane T, Murakami S, Ikeguchi M. Functional Rotation Induced by Alternating Protonation States in the Multidrug Transporter AcrB: All-Atom Molecular Dynamics Simulations. Biochemistry. 2013; 52:7648–7658. [PubMed: 24083838]

26. Khandogin J, Brooks CL III. Constant pH molecular dynamics with proton tautomerism. Biophys J. 2005; 89:141–157. [PubMed: 15863480]

27. Wallace JA, Shen JK. Continuous constant pH molecular dynamics in explicit solvent with pH-based replica exchange. J Chem Theory Comput. 2011; 7:2617–2629. [PubMed: 26606635]

28. Fischer N, Kandt C. Three ways in, one way out: Water dynamics in the transmembrane domains of the inner membrane translocase AcrB. Proteins. 2011; 79:2871–2885. [PubMed: 21905112]

29. Chen W, Morrow BH, Shi C, Shen JK. Recent development and application of constant pH molecular dynamics. Mol Simulat. 2014; 40:830–838.

30. Wallace JA, Shen JK. Predicting p. K_a values with continuous constant pH molecular dynamics. Methods Enzymol. 2009; 466:455–475. [PubMed: 21609872]

31. Alexov E, Mehler EL, Baker N, Baptista AM, Huang Y, Milletti F, Nielsen JE, Farrell D, Carstensen T, Olsson MHM, Shen JK, Warwicker J, Williams S, Word JM. Progress in the prediction of p. K_a values in proteins. Proteins. 2011; 79:3260–3275. [PubMed: 22002859]

32. Wallace JA, Wang Y, Shi C, Pastoor KJ, Nguyen BL, Xia K, Shen JK. Toward accurate prediction of p. K_a values for internal protein residues: the importance of conformational relaxation and desolvation energy. Proteins. 2011; 79:3364–3373. [PubMed: 21748801]

33. Khandogin J, Brooks CL III. Toward the accurate first-principles prediction of ionization equilibria in proteins. Biochemistry. 2006; 45:9363–9373. [PubMed: 16878971]

34. Swails JM, Roitberg AE. Enhancing conformation and protonation state sampling of hen egg white lysozyme using pH replica exchange molecular dynamics. J Chem Theory Comput. 2012; 8:4393–4404. [PubMed: 26605601]

35. Goh GB, Knight JL, Brooks CL. Towards Accurate Prediction of Protonation Equilibrium of Nucleic Acids. J Phys Chem Lett. 2013; 4:760–766. [PubMed: 23526474]

36. Huang Y, Chen W, Dotson DL, Beckstein O, Shen J. Mechanism of pHdependent activation of the sodium-proton antiporter NhaA. Nat Commun. 2016; 7:12940. [PubMed: 27708266]

37. Im W, Feig M, Brooks CL III. An implicit membrane generalized Born theory for the study of structure, stability, and interactions of membrane proteins. Biophys J. 2003; 85:2900–2918. [PubMed: 14581194]

38. Chen W, Huang Y, Shen J. Conformational Activation of a Transmembrane Proton Channel from Constant pH Molecular Dynamics. J Phys Chem Lett. 2016; 7:3961–3966. [PubMed: 27648806]

39. Periole X, Mark AE. Convergence and sampling efficiency in replica exchange simulations of peptide folding in explicit solvent. J Chem Phys. 2007; 126:014903. [PubMed: 17212515]

40. Wilks JC, Slonczewski JL. pH of the Cytoplasm and Periplasm of *Escherichia coli*: Rapid Measurement by Green Fluorescent Protein Fluorimetry. J Bacteriol. 2007; 189:5601–5607. [PubMed: 17545292]

41. Ellis CR, Shen J. pH-Dependent Population Shift Regulates BACE1 Activity and Inhibition. J Am Chem Soc. 2015; 137:9543–9546. [PubMed: 26186663]

42. Jewel Y, Liu J, Dutta P. Coarse-grained simulations of conformational changes in the multidrug efflux transporter AcrB. Mol BioSyst. 2017; 13:2006–2014. [PubMed: 28770910]

43. Takatsuka Y, Nikaido H. Covalently Linked Trimer of the AcrB Multidrug Efflux Pump Provides Support for the Functional Rotating Mechanism. J Bacteriol. 2009; 191:1729–1737. [PubMed: 19060146]

44. Murakami, S. Structures and transport mechanisms of RND efflux pumps. Li, X-Z.Elkins, CA., Zgurskaya, HI., editors. Vol. Chapter 1. Springer; 2016. p. 3-28.

45. Huang Y, Chen W, Wallace JA, Shen J. All-Atom Continuous Constant pH Molecular Dynamics With Particle Mesh Ewald and Titratable Water. J Chem Theory Comput. 2016; 12:5411–5421. [PubMed: 27709966]

46. Brooks BR, Brooks CL III, Mackerell AD Jr, Nilsson L, Petrella RJ, Roux B, Won Y, Archontis G, Bartles C, Boresch S, Caflisch A, Caves L, Cui Q, Dinner AR, Feig M, Fischer S, Gao J, Hodoscek M, Im W, Lazaridis KKT, Ma J, Ovchinnikov V, Paci E, Pastor RW, Post CB, Pu JZ, Schaefer M, Tidor B, Venable RM, Woodcock HL, Wu X, Yang W, York DM, Karplus M.

CHARMM: the biomolecular simulation program. J Comput Chem. 2009; 30:1545–1614. [PubMed: 19444816]

47. MacKerell AD Jr, Bashford D, Bellott M, Dunbrack RL Jr, Evanseck JD, Field MJ, Fischer S, Gao J, Guo H, Ha S, Joseph-McCarthy D, Kuchnir L, Kuczera K, Lau FTK, Mattos C, Michnick S, Ngo T, Nguyen DT, Prodhom B, Reiher WE III, Roux B, Schlenkrich M, Smith JC, Stote R, Straub J, Watanabe M, Wiórkiewicz-Kuczera J, Yin D, Karplus M. All-atom empirical potential for molecular modeling and dynamics studies of proteins. J Phys Chem B. 1998; 102:3586–3616. [PubMed: 24889800]

48. MacKerell AD Jr, Feig M, Brooks CL III. Extending the treatment of backbone energetics in protein force fields: limitations of gas-phase quantum mechanics in reproducing protein conformational distributions in molecular dynamics simulations. J Comput Chem. 2004; 25:1400–1415. [PubMed: 15185334]

49. Klauda JB, Venable RM, Freites JA, O'Connor JW, Tobias DJ, Mondragon-Ramirez C, Vorobyov I, Alexander D, MacKerell Pastor RW Jr. Update of the CHARMM all-atom additive force field for lipids: validation on six lipid types. J Phys Chem B. 2010; 114:7830–7843. [PubMed: 20496934]

50. Jo S, Kim T, Im W. Automated builder and database of protein/membrane complexes for molecular dynamics simulations. PLoS ONE. 2007; 2:e880. [PubMed: 17849009]

51. Wu EL, Cheng X, Jo S, Rui H, Song KC, Dávila-Contreras EM, Qi Y, Lee J, Monje-Galvan V, Venable RM, Klauda JB, Im W. CHARMM-GUI Membrane Builder toward realistic biological membrane simulations. J Comput Chem. 2014; 35:1997–2004. [PubMed: 25130509]

52. Pronk S, Páll S, Schulz R, Larsson P, Bjelkmar P, Apostolov R, Shirts MR, Smith JC, Kasson PM, van der Spoel D, Hess B, Lindahl E. GROMACS 4.5: a high-throughput and highly parallel open source molecular simulation toolkit. Bioinformatics. 2013; 29:845–854. [PubMed: 23407358]

53. Kong X, Brooks C III. Lλ-dynamics: A new approach to free energy calculations. J Chem Phys. 1996; 105:2414–2423.

54. Lee MS, Salsbury FR Jr, Brooks CL III. Constant-pH molecular dynamics using continuous titration coordinates. Proteins. 2004; 56:738–752. [PubMed: 15281127]

55. Im W, Lee MS, Brooks CL III. Generalized Born model with a simple smoothing function. J Comput Chem. 2003; 24:1691–1702. [PubMed: 12964188]

56. Wallace JA, Shen JK. Charge-leveling and proper treatment of long-range electrostatics in all-atom molecular dynamics at constant pH. J Chem Phys. 2012; 137:184105. [PubMed: 23163362]

57. Rathore N, Chopra M, de Pablo JJ. Optimal allocation of replicas in parallel tempering simulations. J Chem Phys. 2005; 122:024111. [PubMed: 15638576]

58. Okur A, Wickstrom L, Simmerling C. Evaluation of salt bridge structure and energetics in peptides using explicit, implicit, and hybrid solvation models. J Chem Theory Comput. 2008; 4:488–498. [PubMed: 26620789]
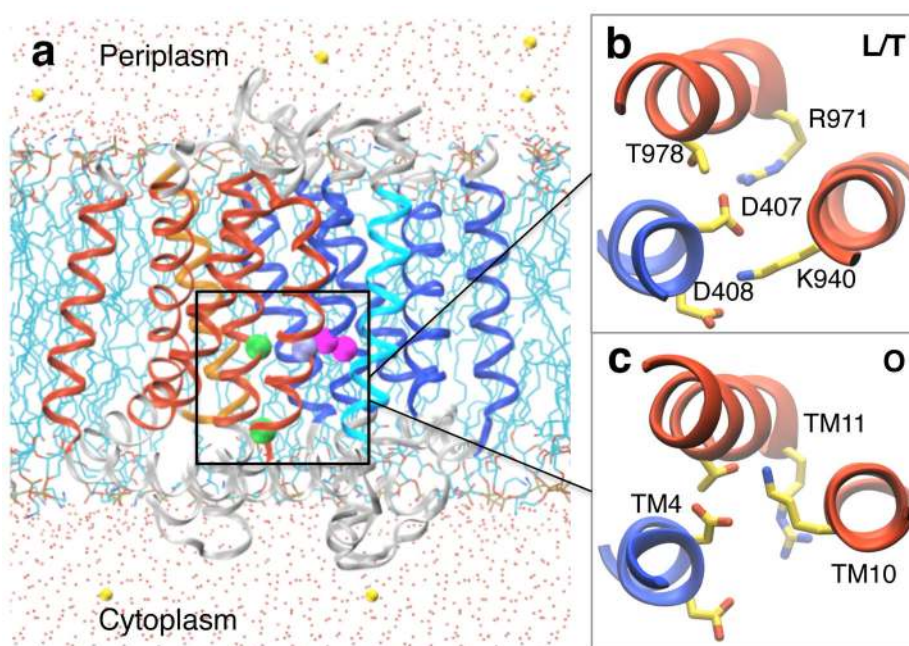
Figure 1. TM domain structure of AcrB and essential residues for proton translocation

a) Sideview of the simulated system. Helices in the N- and C-terminal structural repeats, R1 and R2, are shown in blue and red, respectively. The flanking helices TM2 and TM8 are shown in cyan and brown, respectively. The Cα positions of essential residues Asp407, Asp408, Lys940, Arg971 and Thr978 are highlighted as magenta (Asp), green (Lys/Arg) and silver (Thr) spheres. Water and ions are shown as dots and spheres, respectively. b) Periplasmic view of the essential residues in the L/T protomer. Essential residues are labeled. Note, L and T protomers are nearly identical in the TM domain of AcrB. c) Periplasmic view of the essential residues in the O protomer. Relevant helices are labeled. Coordinates are taken from the crystal structure with pdb id 4DX5.[16]
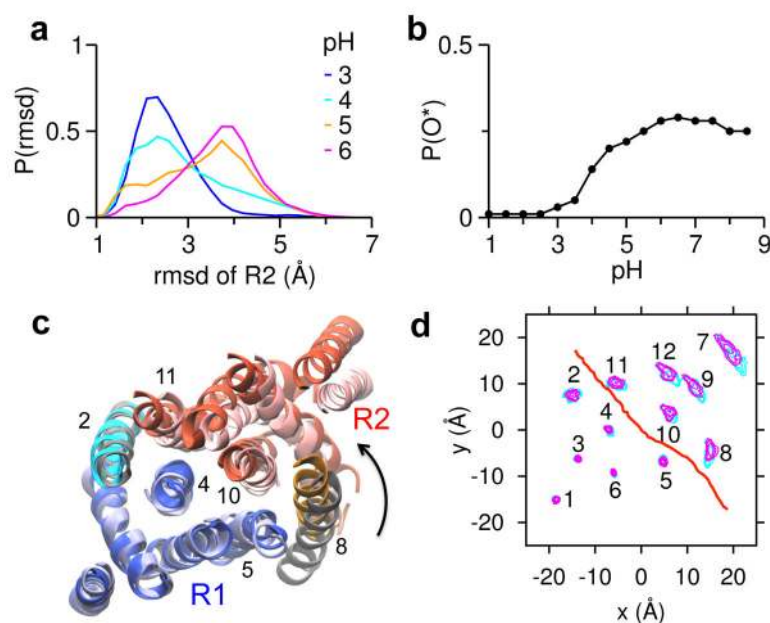
Figure 2. High pH induces a lateral rotation of R2

a) Distribution of the R2 rmsd from the starting structure at different pH. All snapshots were aligned using rms fitting of R1 to the starting structure. R1 includes TM1 and TM3–TM6, while R2 includes TM7 and TM9–TM12. b) Occupancy of O^* state (defined using an rmsd cutoff of 4 Å) at simulated pH conditions. c) Periplasmic view of the overlaid representative snapshots of O (lighter colors) and O^* state (darker colors). For the latter, R1 and R2 helices are colored blue and red, respectively. Flanking helices TM2 and TM8 are colored cyan and brown, respectively. Helices discussed in the main text are labeled. d) Centers of mass of TM helices projected on the membrane plane following the alignment of R1. Data at pH 4 and 6 are shown in cyan and magenta, respectively. A red curve separates the R1 and R2 repeats.
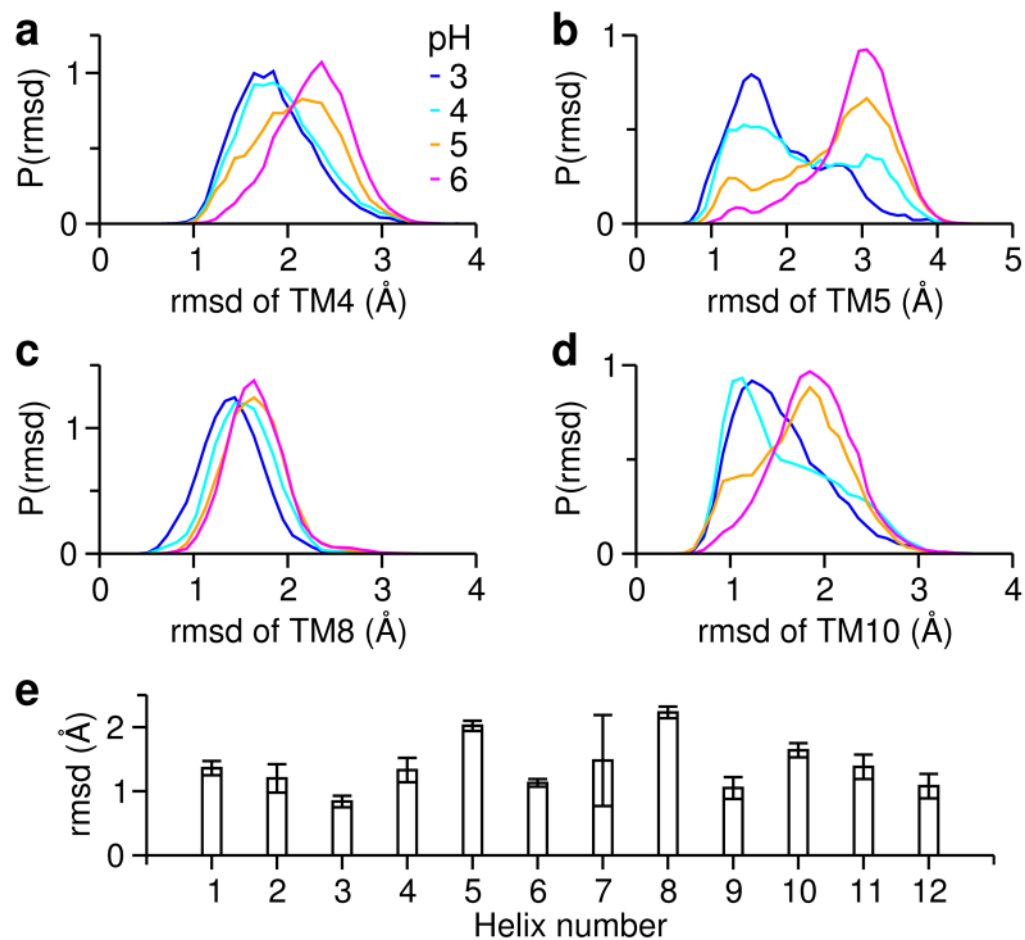
Figure 3. High pH induces backbone conformational changes in TM4, TM5, TM8 and TM10

a–d) Distribution of the backbone rmsd of TM4, TM5, TM8 and TM10 at different pH. All TM helices were aligned to the starting structure. e) Backbone rmsd between the L and O protomers for individual TM helices in the crystal structures (see Table S3 for more details).
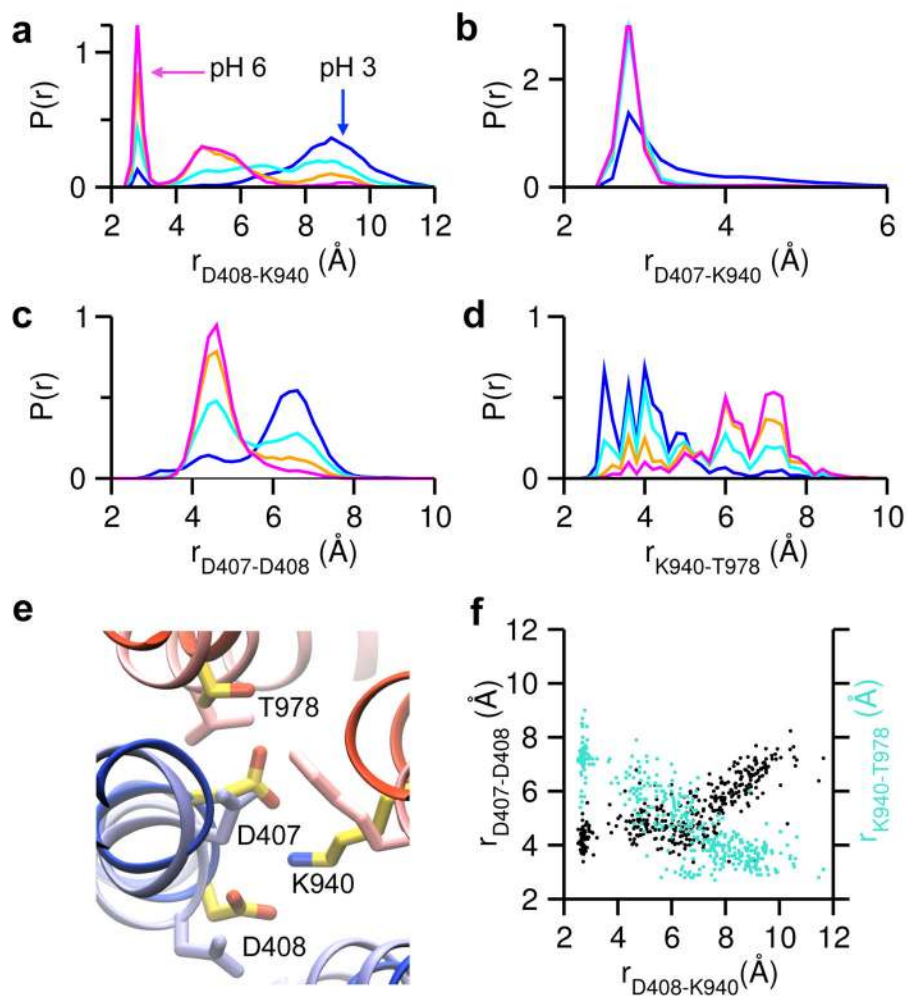
Figure 4. High pH induces sidechain rearrangements of essential residues

a–d) Distribution of the minimum sidechain distance between Asp408 and Lys940, Asp407 and Lys940, Asp407 and Asp408 as well as between Lys940 and Thr978. The minimum sidechain distance was measured using carboxylate oxygen (Asp), amine nitrogen (Lys) and hydroxyl oxygen (Thr). Trajectories at pH 3, 4, 5 and 6 are shown in blue, cyan, orange and magenta, respectively. e) Zoomed-in view of sidechain interactions in O (colored blue and pink) and O* (colored based on atom types) states. f) Instantaneous minimum sidechain distance of Asp408 to Lys940 *vs.* that of Asp407 to Asp408 (black) and that of Lys940 to Thr978 (turquoise). Data taken from the pH 4.5 trajectory.
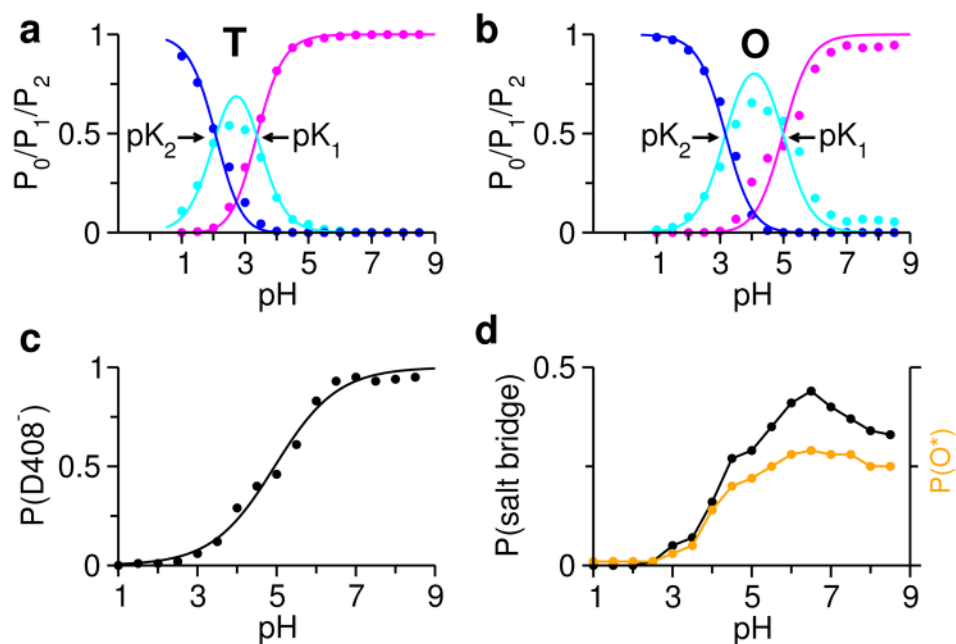
Figure 5. Titration of Asp407/Asp408

a) Stepwise protonation of the Asp407/Asp408 dyad in the T state. P_0, P_1 and P_2 represent the probability of having 0 (magenta), 1 (cyan) and 2 (blue) protons. Curves are the best fits to the stepwise titration model. The stepwise pK_a's are the cross points of the curves. b) Stepwise protonation of the Asp407/Asp408 dyad in the O state. c) Fraction of deprotonated Asp408 in the O state as a function of pH. Curve is the best fit to the Hill equation. d) Probability of the salt bridge formation between Asp408 and Lys940 as a function of pH (black). Occupancy of the O* state as a function of pH (orange). A salt bridge was defined using a minimum sidechain distance cutoff of 4 Å.
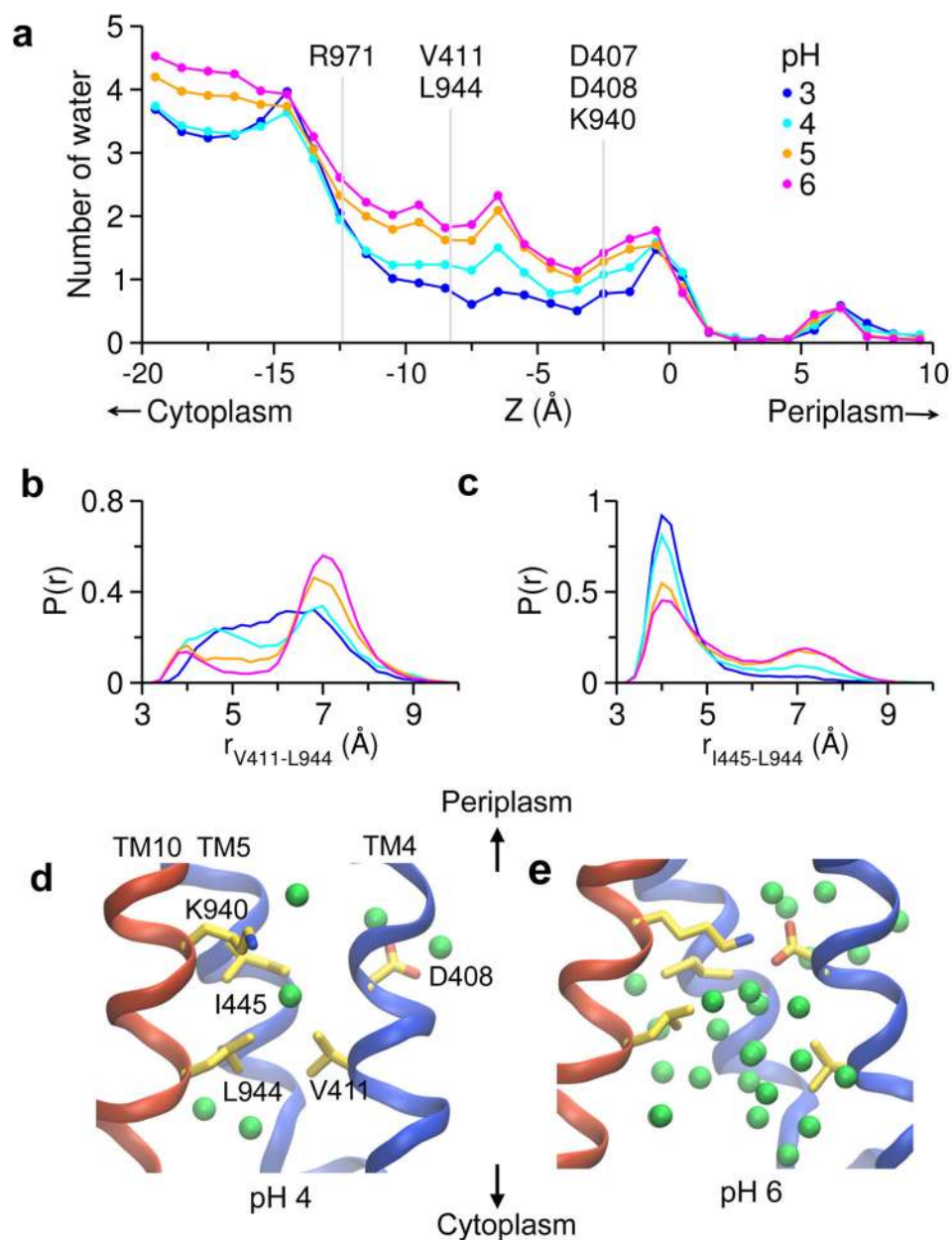
Figure 6. Disruption of hydrophobic contacts allows water to access the proton binding site
a) Number of water along the membrane normal (z) at different pH. The number of water oxygen atoms was counted in 1- Å slices within a radius of 10 Å centered the z axis. The z positions of residues discussed in the main text are indicated in grey. b) Distribution of the minimum sidechain heavy atom distance between Val411 and Leu944 at different pH. c) Distribution of the minimum sidechain heavy atom distance between Ile445 and Leu944 at different pH. d,e) Snapshots taken from trajectories at pH 4 and pH 6. Sidechains of Asp408, Val411, Ile445, Lys940 and Leu944 are shown in stick model. Water within 4.5 Å are shown as green spheres.
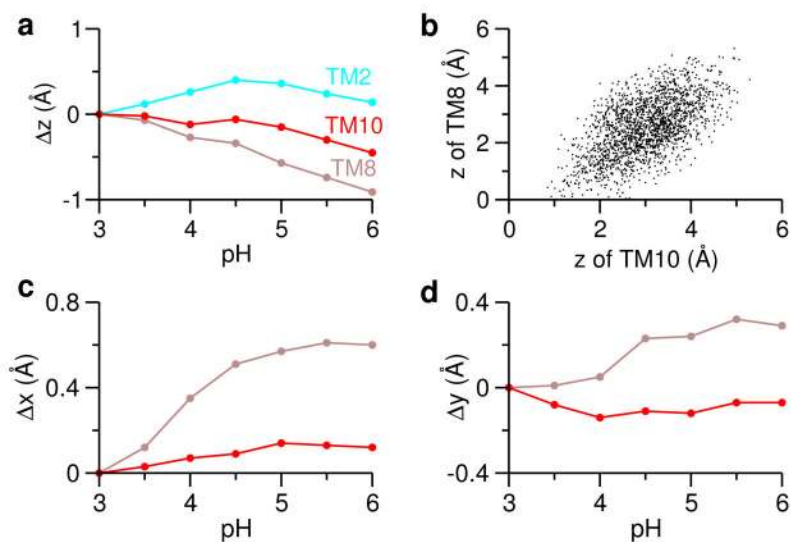
Figure 7. TM8 appears to move towards cytoplasm at increasing pH
a) pH-dependent change of the center-of-mass (COM) z position of TM2, TM8 and TM10 in reference to pH 3. b) Instantaneous COM z position of TM8 *vs.* that of TM10. c) pH-dependent change of the COM x position of TM8 and TM10 in reference to pH 3. d) pH-dependent change of the COM y position of TM8 and TM10 in reference to pH 3. For clarity, only the average positions are displayed in a, c, and d; the root-mean-square fluctuations are given in Fig. S15.
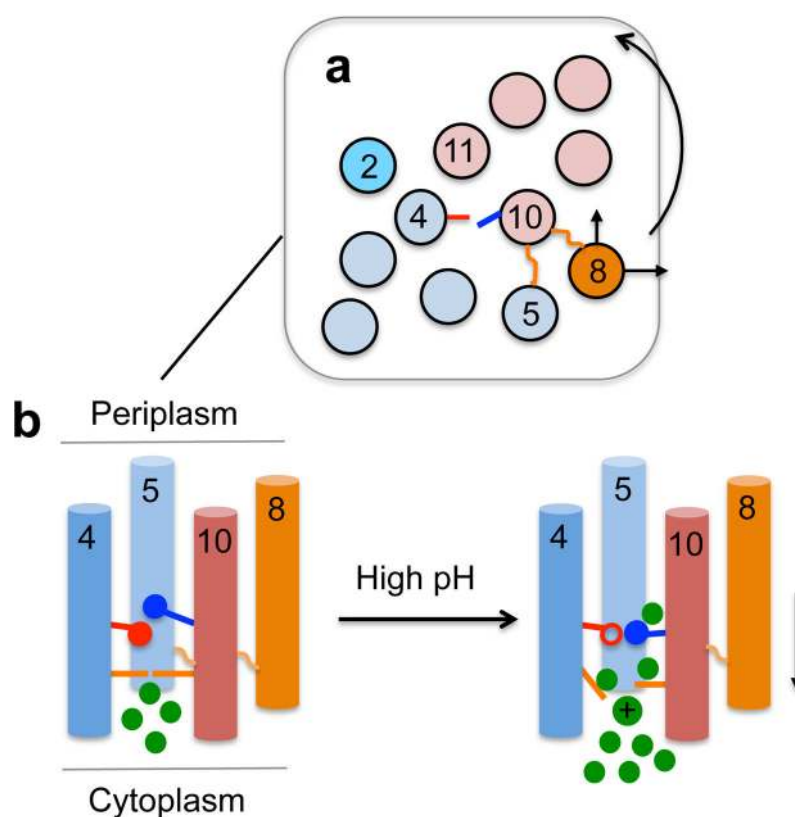
Figure 8. Cartoon representation of the pH-induced conformational changes revealed by the simulations of the O protomer

a) Top (periplasmic) view of the TM domain. Circles represent the TM helices, red for R1 and blue for R2 repeat. TM2 and TM8 are colored cyan and orange, respectively. Important helices are labeled. The lateral rotation of R2 about R1 as well as the movement of TM8 in x and y directions are indicated by arrows. Asp408, Lys940 as well as hydrophobic interactions are indicated. b) Side view of the TM helices showing major conformational changes in the simulation. Asp408 and Lys940 are colored red and blue, respectively. Open circle indicates the deprotonated state. Hydrophobic contacts are represented by orange sticks. Water molecules are shown as green spheres (the one carrying a proton is indicated with a plus sign). Vertical movement of TM8 is indicated by an arrow.

Table 1

Calculated pK_a's of Asp407/Asp408 in the L, T, O and O* states

	L	T	O	O*
D407/D408[a]	2.2/3.0	2.6/2.8	3.4/5.0	2.6/3.1
First/second[b]	3.4/1.9	3.4/2.1	5.0/3.2	3.0/2.6

[a] Microscopic pK_a's of Asp407 and Asp408. The block standard errors (BSE) for the microscopic pK_a's in the L/T, O, and O* states are 0.1, 0.15 and 0.3, respectively.

[b] Macroscopic pK_a's of the first/second protonation events of the aspartic dyad. The O and O* states were defined as those snapshots with an R2 rmsd below 2 and above 4 A, respectively.